

Initial Characterization of the SAFIR Prototype PET-MR Scanner

Christian Ritzer¹, Robert Becker, Alfred Buck, Volker Commichau, Jan Debus, Lubomir Djambazov, Afroditi Eleftheriou, Jannis Fischer², Peter Fischer, Mikiko Ito, Parisa Khateri, Werner Luster mann, Michael Ritzert, Ulf Röser, Markus Rudin³, Ilaria Sacco, Charalampos Tsoumpas⁴, Geoffrey Warnock, Matthias Wyss⁵, Agnieszka Zagodzinska-Bochenek, Bruno Weber, and Günther Dissertori

Abstract—The SAFIR collaboration is currently developing a high-rate positron emission tomography (PET) insert to study fast kinetic processes in small animals. Our insert is designed for simultaneous image acquisition with a preclinical 7 T magnetic resonance (MR) imaging device. In contrast to existing preclinical PET scanners and inserts, our hardware is optimized for high-rate measurements with source activities up to 500 MBq. As a first step, the SAFIR Prototype insert was constructed. This already incorporates the final components, but has a reduced axial field-of-view (35.6 mm). We use lutetium-yttrium oxyorthosilicate crystals (2.12 mm × 2.12 mm × 13 mm) one-to-one coupled to silicon photomultipliers. All analog signals are digitized within the insert. We use 49 MR-compatible dc-dc converters in the insert to provide the power to all readout electronics. After shimming, no degradation of the homogeneity of the static B_0 field in the MR scanner was observed. During full operation, we saw a minor reduction in the signal-to-noise ratio of the MR data of 4.9%. With a low activity point source (^{22}Na 0.65 MBq) we obtained a coincidence energy resolution of 13.8% full width at half maximum (FWHM) and a coincidence timing resolution of 194 ps (FWHM). First PET/MR rat brain and high-rate mouse cardiac images (84.9 MBq) are shown in this article.

Manuscript received August 4, 2019; revised November 15, 2019, December 29, 2019, and February 23, 2020; accepted February 27, 2020. Date of publication March 18, 2020; date of current version September 2, 2020. This work was supported by the ETH Zurich Foundation through ETH Research under Grant ETH-30 14-2. The work of Charalampos Tsoumpas was supported by the Royal Society Industry Fellowship under Grant IF170011. The work of Geoffrey Warnock was supported by the Clinical Research Priority Program for Molecular Imaging of the University of Zurich. (Corresponding author: Christian Ritzer.)

Christian Ritzer, Robert Becker, Volker Commichau, Lubomir Djambazov, Jannis Fischer, Mikiko Ito, Parisa Khateri, Werner Luster mann, Ulf Röser, Agnieszka Zagodzinska-Bochenek, and Günther Dissertori are with the Institute for Particle Physics and Astrophysics, ETH Zürich, 8093 Zürich, Switzerland (e-mail: critzer@phys.ethz.ch).

Alfred Buck is with the Clinic of Nuclear Medicine, University of Zürich, 8057 Zürich, Switzerland.

Jan Debus, Peter Fischer, Michael Ritzert, and Ilaria Sacco are with the Institute of Computer Engineering, University Heidelberg, 69117 Heidelberg, Germany.

Afroditi Eleftheriou, Geoffrey Warnock, Matthias Wyss, and Bruno Weber are with the Institute for Pharmacology and Toxicology, University of Zürich, 8057 Zürich, Switzerland.

Markus Rudin is with the Institute for Biomedical Engineering, ETH Zürich, 8092 Zürich, Switzerland.

Charalampos Tsoumpas is with the Leeds Institute of Cardiovascular and Metabolic Medicine, University of Leeds, Leeds LS2 9NL, U.K.

Color versions of one or more of the figures in this article are available online at <http://ieeexplore.ieee.org>.

Digital Object Identifier 10.1109/TRPMS.2020.2980072

Index Terms—High rate PET, instrumentation, molecular imaging, multimodality imaging, positron emission tomography (PET)/magnetic resonance (MR), preclinical PET insert, SAFIR, TOF-PET.

I. INTRODUCTION

THE SAFIR collaboration was formed to develop a positron emission tomography (PET) insert for an existing preclinical magnetic resonance (MR) imaging system (Bruker BioSpec 70/30) [1], [2]. The insert is designed for very high count rate measurements, enabling image acquisition times of less than 5 s [3]–[5], something that in humans has become possible only recently with the development of the total body PET scanner [6]. The target activity in the field-of-view is 500 MBq, which leads to hit rates of about 60 kHz per crystal. In order to handle these data rates, a one-to-one coupling for the lutetium-yttrium oxyorthosilicate (LYSO) crystals and the silicon photomultipliers (SiPMs) was specified. The requirements for the detector are based on GATE simulations [2].

- 1) *Spatial Resolution*: <2 mm.
- 2) *Coincidence Timing Resolution (CTR)*: <300 ps.
- 3) *Energy Resolution*: <20%.

In this article, we focus on the coincidence energy resolution (CER), the CTR, and the MR-compatibility. Furthermore, we show the first high rate images and our first combined PET-MR image. The geometric dimensions of the constructed PET insert are summarized in Table I.

II. MATERIALS

The SAFIR Prototype insert has the shape of a hollow cylinder with an inner (outer) diameter of 114 mm (199 mm) and an overall length of 103 cm. The mechanical support structure is made of carbon fiber. Internally, the insert comprises 12 identical sectors on an equilateral dodecagon. On each face of this dodecagon, a carbon fiber casket is mounted, housing the digital interface board equipped with two detector modules. The detector has an axial field of view of 35.6 mm and the distance between the front faces of opposing crystals is

TABLE I
DIMENSIONS OF THE SAFIR PROTOTYPE PET-MR SCANNER

Axial field of view (FOV)	35.8 mm
Transverse FOV with / without MR coil	72 mm / 114 mm
# crystals	$16 \times 180 = 2880$
Crystal size	$2.12 \times 2.12 \times 13 \text{ mm}^3$
Crystal pitch	2.2 mm
SiPM pixel size	$2.0 \times 2.0 \text{ mm}^2$
Outer diameter	199 mm
Length	103 cm

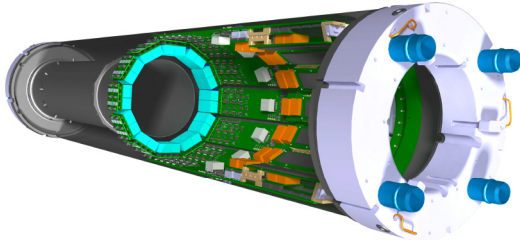


Fig. 1. Rendering of the SAFIR Prototype insert.

128 mm. At the end of the detector there are fast signal distribution boards and power distribution boards. A rendering of the insert is shown in Fig. 1.

A. HF Shielding

We use three different RF shields in the SAFIR Prototype insert. The innermost layer is the carbon fiber cylinder, with 2-mm wall thickness. It is followed by a copper-Kapton multilayer shield. This comprises 25-mm wide stripes of copper (35- μm thickness) and Kapton tape (69- μm thickness). The different layers overlap by 12.5 mm. This shield covers the central area of the insert (20-cm long). Finally, there are the carbon fiber caskets, that house the electronics. All carbon fiber material is made with graphite enriched epoxy glue.

B. Detector Module

The detector module comprises a readout board, two SiPM arrays and two LYSO crystal matrices (Tianle Photonics). The crystals are one-to-one coupled to the SiPMs. Crystals of $2.12 \text{ mm} \times 2.12 \text{ mm} \times 13 \text{ mm}$ are used and arranged in crystal arrays of 7×8 and 8×8 crystals with a pitch of 2.2 mm. The crystals within each array are optically separated by enhanced specular reflector foil (3M Vikuiti Enhanced Reflector Films). The arrays are glued onto SiPM matrices made of 8×8 pixels with $2 \text{ mm} \times 2 \text{ mm}$ pixel size and 2.2 mm pixel pitch (Hamamatsu TSV MPPC array S13361-2050AX-08). The custom SiPM arrays provide readout of all cathodes while having common anodes. Thus, their negative signal polarity matches the readout application-specific integrated circuits (ASICs) employed. Each readout board carries four ASICs, two per SiPM array. We use the PETA6SE-ASIC designed by Prof. Fischer and his group from the University of Heidelberg as readout ASIC [7], [8]. It has 36 single-ended input channels, a size of $5 \text{ mm} \times 6 \text{ mm}$ and is flip-chip bondable. The ASIC amplifies the pulse of the SiPM and uses a

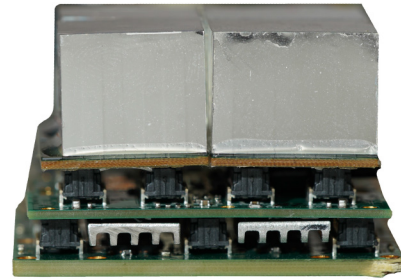


Fig. 2. Picture of the detector module (top to bottom): LYSO crystal matrices, SiPM arrays, the readout board hosting four flip-chip bonded PETA6SE ASICs (covered by two heatsinks), and the end of the digital interface board.

time-to-digital-converter (TDC) comprising a fine counter (bin width 50 ps) and a coarse counter (bin width 1.6 ns) together with a fast leading edge discriminator to measure the arrival time of the SiPM signals. Eighteen channels share one TDC. In addition, a charge-to-digital-converter (QDC) measures the signal charge. The ASIC needs about 33-mW input power per channel and operates at 1.8 V. Two differential data transmission lines per ASIC, operating at 200 MHz, are used to transfer the digitized data to the digital interface board. An image of the readout board is shown in Fig. 2. In total there are 2880 crystals and 3072 SiPM pixels in the insert.

C. Digital Interface Board

There is one digital interface board in each sector, thus, 12 in total. The functions of the digital interface board are: data transfer from the ASICs to the data acquisition (DAQ) computer, ASIC configuration and slow control. We employ an FPGA (Xilinx Kintex 7 “XC7K70T-2FBG484I”) and an optical Ethernet link, operated at 1 GBit/s [9]. Within the Kintex FPGA, we use a softcore microcontroller (MircoBlaze) for the slow control tasks. These include temperature measurement and communication with the bias voltage system. For the temperature measurement, there are five onboard sensors (LTC 2990) below the five slots for readout modules [10]. An image of the digital interface board, together with two detector modules and a bias generation board is shown in Fig. 3. Their interplay is illustrated in Fig. 4.

D. Power Distribution and Conversion

The digital electronics in the SAFIR Prototype insert is supplied by a single power supply, placed outside of the Faraday cage. It provides power at 16 V DC and is connected via 11 m long cables (10 m with 6 mm^2 and 1 m with 2.5 mm^2) with the primary power distribution boards inside the insert. These boards have reverse voltage protection diodes and transient-voltage-suppression diodes to protect the detector from incorrect operation and distribute the voltage further to the secondary power distribution boards (one in each casket). We developed MR-compatible dc-dc converter modules, to generate all required voltages inside our detector [11]. The dc-dc converters take any input voltage from 6 V to 20 V and transform it to the intermediate voltages of 2.4 V and 4.1 V. In total, we have 49 dc-dc converters installed inside the insert. They supply linear low-dropout regulators, providing

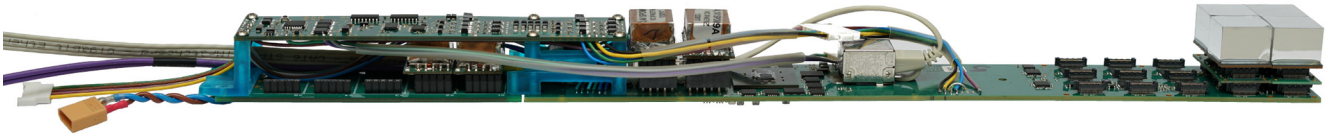


Fig. 3. All electronics from one casket (from left to right): secondary power distribution board (bottom left), bias generation board (top), one digital interface board and two detector modules (top right).

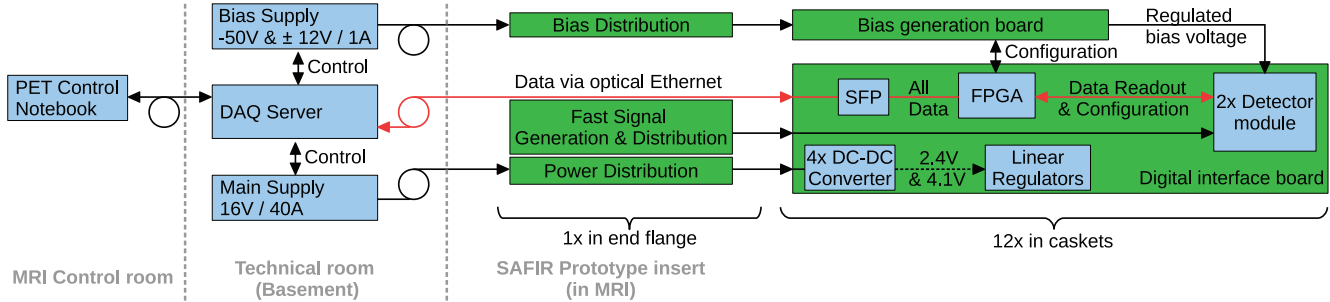


Fig. 4. Interplay of the boards within the insert and with the infrastructure outside of the MR room. The data path is marked in red.

all voltages (1 V–3.3 V) for the components. The conversion efficiency of our dc–dc converter modules is 85% and the total input power of our insert is about 300 W.

E. Bias Generation

We use three different voltages (-50 V; ± 12 V) for the bias system, which are brought into the insert from three independent power supplies, placed outside of the MR-room. These are fed into the bias distribution boards, which, in turn, supply 12 bias and temperature (SBT) boards, one per sector. The SiPMs need a bias supply of about -58 V. The bias voltage is composed of a fixed shift voltage of -50 V, stabilized with remote sensing and an adjustable part of 0 V to -10 V provided by the SBT board. Each SBT board has six independent output channels. We use one bias channel for each detector module and both SiPM arrays on the module are selected to have approximately the same break down voltage. In addition, there is the possibility to correct the bias voltage of each SiPM channel from within the ASIC, a feature which was not used for the results presented in this article. Overall, the bias system has an absolute accuracy of 85 mV, which is similar to the typical spread of the break down voltages of the 64 SiPMs in one array. We operate all SiPMs with an overvoltage of 6 V.

F. Fast Signal Generation and Distribution

We have three fast control signals in our detector system. These are the 25-MHz system clock, the synchronization signal, and the test-trigger signal. All signals are transmitted via low voltage differential signaling (LVDS) connections throughout our insert. There is one fast control master board, generating these signals. It is connected to two fast control distribution boards, which distribute them to the digital readout boards. On the digital readout boards, the signals are distributed further to all attached ASICs on the detector modules. All interconnections for the fast control signals use standard Ethernet cables with RJ45 connectors.

G. Cooling System

The SAFIR Prototype insert employs forced air cooling. We use a 2.2-kW side-channel blower (SCL K05-MS-2.2kW) to suck air through the detector. The blower is placed in the technical room and operates continuously at full power. It is connected via plastic tubing (45-mm inner diameter, 10-m length) with four hoses (20-mm inner diameter, 1-m length) coming out at one end of the insert. On the other side, ambient air (20 °C) flows into the insert. The fresh air first passes the SiPMs and ASICs, followed by the rest of the electronics.

H. MR System

We use a “Bruker BioSpin 70/30 MRI” system together with a “B-GA20S” gradient system. The gradient system has an inner diameter of 200 mm, a maximum gradient strength of 200 mT/m and a maximum slew rate of 640 T/m/s. For all phantom measurements, we used a mouse size volume coil (Bruker “RF RES 300 1H 075/040 QNS TR”). In addition, we used a rat size volume coil (Bruker “RF RES 300 1H 112/72 QNS TR M”) for the simultaneous PET/MR animal images.

III. METHODS

A. Temperature Measurement

The onboard temperature sensors are read out once per second. We record all temperature values together with other slow control data for offline analysis. Ten temperature measurements are used to calculate the mean temperature over a 10 s period.

B. Data Processing

The raw data from the insert are saved on the DAQ computer and all processing is done offline. We apply calibration data (see next section) to get singles and afterward we use a single-window coincidence sorter (500 ps coincidence window time) to obtain coincidences. Coincidences consisting of more than two singles are rejected (if no intercrystal scatter recovery is

active). All coincidences are filtered with an energy window (standard: 391 keV–601 keV). A cut on the tangential angle between the singles ($<90^\circ$) is applied. There is the possibility to recover triple coincidences (see below). If intercrystal scatter recovery is used, we apply the energy window and the tangential cut on the recovered singles.

C. Data Calibration

We use the measurement from a ^{22}Na point source positioned in the center of the field of view to obtain energy and timing delay calibration data. To get the energy E (in keV) from the measured QDC value, we use a logarithmic model

$$E = \alpha_c(\text{QDC} - \beta_c)^{\gamma_c}$$

with three constants α_c , β_c , and γ_c , that depend on the channel c . The offset β_c is derived from a test-trigger measurement. The other two constants are derived from ^{22}Na data. We determine the position of the 511 keV and the 1275 keV peaks and analytically calculate α_c and γ_c .

The timing delay calibration is done in two steps using the point source measurement data. First, we process it with a wide coincidence window (5 ns), cut on the photopeak (391 keV–601 keV) and combine all 16 channels of one TDC. We use the mean value m_{ij} of the time difference of each TDC pair i, j together with its standard deviation s_{ij} , and the number of coincidences n_{ij}

$$\sum_{ij} \frac{(m_{ij} - d_i + d_j)^2}{s_{ij}^2 n_{ij}}.$$

We minimize this sum and obtain the delay values d_i and d_j for the TDCs.

Afterward, the same procedure is repeated with a narrower coincidence window (1.5 ns) for all crystals. The delay values from the TDC calibration are applied and the same energy window (391 keV–601 keV) is used. Before the minimization, we filter on the number of coincidences per crystal pair (min. 50), in order to increase the stability of the calibration routine. More than 1 million coincidences were used in total for this calibration.

Moreover, we use the point source measurement data to calibrate the energy-dependent delay caused by the leading edge discriminator (time-walk effect) [12]. We correct the time stamps of the singles by Δt based on the measured energy E using

$$\Delta t = \kappa(E - 511 \text{ keV})^2$$

with a global constant κ . We process the dataset with all delay calibration data applied, a large energy window (211 keV–661 keV) and a 500-ps coincidence window. Additionally, we filter the energies of the coincidences, so that one single always is on the photopeak (461 keV–561 keV). We analyze the time difference with respect to the energy of the other single and obtain κ from a fit to this distribution. The calibration data are saved and reused for all other measurements.

D. Intercrystal Scatter Recovery

Intercrystal scatter recovery is performed after coincidence search. In coincidences with three hits, we look for pairs of hits that are closer together than a specified distance, called recovery range (typically 3.5 mm or 5 mm). The two interactions are merged into a single. We have tested different methods to combine the interactions and selected the one with the most accurate crystal assignment, measured by the average minimum distance of the lines of response to the source position. We select the interaction with the higher energy as primary interaction. The second interaction is removed and its energy is added to the primary interaction. The time stamp is generated by the weighted mean of the two time stamps, with their individual energy values as weights (to account for the different photon statistics). The time stamp of the second interaction is corrected for the flight time of the scattered gamma ray between the crystals. At the end, the final energy window and the cut on the minimum separation in tangential direction is applied on the recovered data.

E. Data Analysis

We report the energy resolution and timing resolution after coincidence search. For the analysis of the CER, we fitted a Gaussian function over the interval from 480 keV to 580 keV to the coincidence energy spectrum. We report the full width at half maximum (FWHM) of the fitted function. To obtain the CTR from the timing spectrum, we select the highest bin and fit a parabola through it and its two neighbors. The peak of the parabola is used as maximum. Afterward, we interpolate between the bins of the coincidence timing spectrum at half the maximum to obtain the FWHM value of the measured distribution. The number of all lines of response that are not more than 10 mm away from the source is reported in addition. We analyse the same dataset with different energy windows as well as with intercrystal scatter recovery. If intercrystal scatter recovery is enabled, we first use a wide energy window (100 keV–601 keV) for the coincidence search and apply the final energy window (391 keV–601 keV) on the recovered data.

F. Image Reconstruction

We save all coincidences in the form of listmode files. Image reconstruction is then performed using a standard ordered subset expectation maximization algorithm [13]. The system matrix is calculated by ray-tracing, with 15 625 rays per line of response. We use a voxel size of 0.733 mm \times 0.733 mm \times 0.733 mm (1/3 of the crystal pitch) and create images of 120 \times 120 \times 60 voxels. In total 12 iterations are used, with 12 subsets each. After every full iteration a Gaussian filter with an FWHM of 1.467 mm (2/3 of the crystal pitch) was applied to smooth the image [14].

G. PET Images

All raw data were stored and processed offline with an energy window from 391 keV to 601 keV, 500-ps coincidence timing window and no intercrystal scatter recovery was

applied. The presented images are slices with a thickness of one voxel (0.733 mm) and they are zoomed by a factor of ten with linear interpolation. The image fusion of the PET and MR images is performed using commercially available software (PMOD Technologies LLC). We show three different measurements.

- 1) *Mouse Sized Hot Rod Phantom*: 1.5 MBq/mL ^{18}F , 150 s acquisition time, four different rod-diameters (1.4 mm, 1.5 mm, 1.7 mm, 2.0 mm) and a rod-center to rod-center distance of twice their diameter.
- 2) *Ex Vivo Rat Brain*: 37.3 MBq ^{18}F -labeled-tracer (undisclosed), two bed positions with 700 s and 900 s acquisition time, with simultaneous MR acquisition at 2 h after injection, MR sequence: T2 turboare 3-D.
- 3) *In Vivo Mouse Cardiac*: 84.9 MBq ^{18}F -labeled tracer (undisclosed), 1800 s total acquisition time, sample frame reconstructed for a duration of 5 s at 1200 s after injection

H. B_0 Field Distortions

For this measurement, we used a cylindrical and homogeneous phantom filled with a Bruker calibration solution (H_2O , with 1 g/L CuSO_4 and 3.6 g/L NaCl). We measured two B_0 maps ($40\text{ mm} \times 40\text{ mm} \times 40\text{ mm}$, voxel size: $0.5\text{ mm} \times 0.5\text{ mm} \times 0.5\text{ mm}$) following shimming of the MR system. One map is taken without the SAFIR Prototype insert and the other one with the insert. Three central slices are shown in the result section.

I. HF Distortions

This measurement was performed after the shimming of the MR system. We used the same phantom as for the B_0 field distortions measurement together with the Bruker Quality Assurance-SNR protocol. This is based on a T1-weighted sequence with an automatic post-processing. The output is the signal-to-noise ratio (SNR) normalized to the voxel volume. Five repetitions of this measurement were acquired. We report the mean value and standard deviation. To investigate the effect of our insert, we repeated this measurement five times: 1) without the insert; 2) with the insert switched off; 3) after start up in a low power state; 4) during idle operation at full power; and 5) during data acquisition.

J. Influence of the MRI on the PET Count Rate

For this measurement a point source was placed on the animal bed, positioned in the isocenter of the PET insert in the MR system. A mouse volume coil (Bruker “RF RES 300 1H 075/040 QNS TR”) covered the source, as well as a small water phantom. PET data was acquired while different MR sequences were running. The measurement time was 100 s per data point. The data was processed with a single-window coincidence sorter, an energy window from 391 keV to 601 keV, 500-ps coincidence window time and a minimum tangential separation of the hits in one coincidence of $\varphi > 90^\circ$. We compare the coincidence rate for different sequences with a reference measurement in the B_0 field.

TABLE II
AVERAGE BOARD TEMPERATURES

Board	Average temperature over 40 min
# 0	$(26.72 \pm 0.02)^\circ\text{C}$
# 1	$(26.98 \pm 0.02)^\circ\text{C}$
# 2	$(27.09 \pm 0.02)^\circ\text{C}$
# 3	$(25.92 \pm 0.02)^\circ\text{C}$
# 4	$(25.59 \pm 0.01)^\circ\text{C}$
# 5	$(26.33 \pm 0.02)^\circ\text{C}$
# 6	$(26.37 \pm 0.02)^\circ\text{C}$
# 7	$(26.48 \pm 0.02)^\circ\text{C}$
# 8	$(25.94 \pm 0.02)^\circ\text{C}$
# 9	$(26.47 \pm 0.02)^\circ\text{C}$
# 10	$(26.40 \pm 0.02)^\circ\text{C}$
# 11	$(25.75 \pm 0.02)^\circ\text{C}$

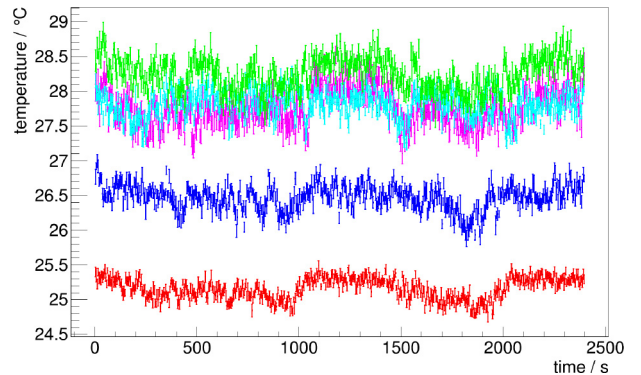


Fig. 5. Measured temperature values (10 s average) for the five sensors on board 2 (warmest board).

IV. RESULTS

A. Temperature Measurements

The average board temperatures are summarized in Table II. The maximum average temperature was 27.09°C and the minimum average temperature was 25.59°C . The measured temperature values for board 2 over a time of 40 min are shown in Fig. 5. There is no overall trend visible. The sensor (red) below the first detector module closest to the air intake was about 3°C colder than the other sensors. The sensor (green) furthest away from the air intake measured the highest temperatures. The temperatures are very stable within one degree Celsius. With an external thermometer, we measured a temperature difference of 5°C between the air intake of the insert and the air outlet of the insert.

B. Coincidence Energy and Timing Spectrum

The measured coincidence energy spectrum for all channels is shown in Fig. 6. The FWHM obtained from the Gaussian fit is 13.8%. The minimum between the photopeak and the Compton edge was at an energy of around 390 keV.

The measured coincidence timing spectrum (energy cut: 391 keV–601 keV) for all channels combined is shown in Fig. 7. The plot contains the measured time differences of all recorded coincidences. The FWHM obtained for the CTR was 194 ps. This is equivalent to an average singles timestamp precision of $(194\text{ ps}/\sqrt{2}) = 137\text{ ps}$ (FWHM) corresponding to $\sigma_{\text{single}} = 58\text{ ps}$.

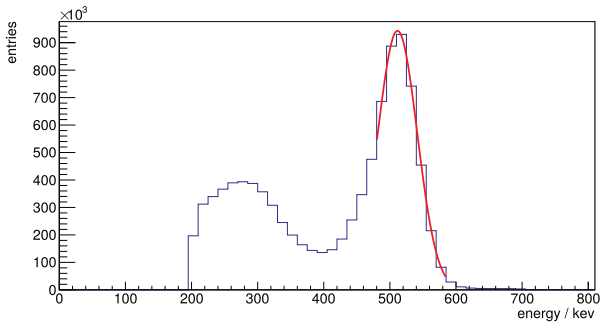


Fig. 6. Measured coincidence energy spectrum from 200 keV to 700 keV.

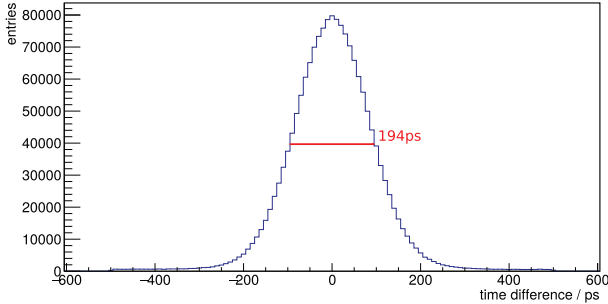


Fig. 7. Measured coincidence timing spectrum for an energy window of 391 keV–601 keV.

TABLE III
CTR FOR DIFFERENT ANALYSIS SETTINGS, ICSR = INTERCRYSTAL SCATTER RECOVERY

Analysis	CTR FWHM	# Coincidences
200 keV – 700 keV	219 ps	4.48×10^6
250 keV – 700 keV	213 ps	3.78×10^6
350 keV – 650 keV	198 ps	1.94×10^6
391 keV – 601 keV	194 ps	1.68×10^6
391 keV – 601 keV + ICSR 3.5 mm	205 ps	2.37×10^6
391 keV – 601 keV + ICSR 5.0 mm	205 ps	2.57×10^6
391 keV – 601 keV + ICSR 8.0 mm	205 ps	2.73×10^6

C. Results for Intercrystal Scatter Recovery

For this analysis, the data of the same dataset were processed with different settings, according to Table III. As comparison to the results for the intercrystal scatter recovery we present results for wider energy windows without intercrystal scatter recovery, too. The intercrystal scatter recovery decreased the CTR from 194 ps to 205 ps. The benefit was an increase of about 41%–63% in the number of detected coincidences.

D. B_0 Field Distortions

The measured B_0 maps are shown in Fig. 8. The maximum deviations were around 0.1 ppm in the shimmed area (a cylinder of 26-mm diameter and 15-mm length, to fit the phantom) and 0.7 ppm at the edges of the field of view.

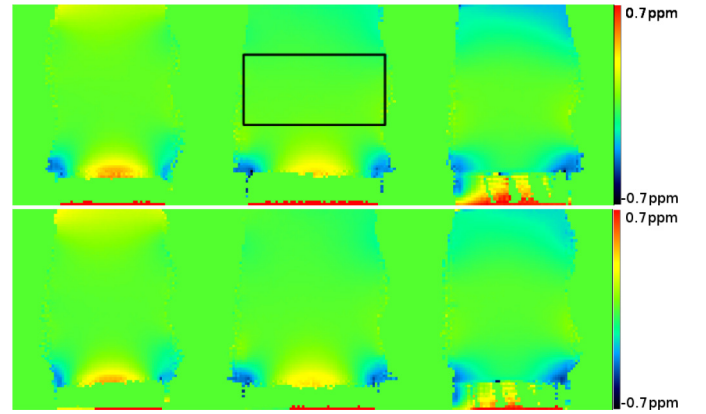


Fig. 8. Three representative slices from B_0 maps with/without SAFIR. Slices 20, 40, 60 from 80 slice acquisition (80×80 matrix size in plane). Top: B_0 map without SAFIR, after shimming; Bottom: B_0 map with SAFIR, after shimming. The black box indicates the shimmed region.

TABLE IV
NORMALIZED SNR VALUES FOR DIFFERENT OPERATING CONDITIONS

Operating Condition	Normalized SNR	Deviation
a) Baseline (no insert)	$(3968 \pm 18) \text{ mm}^{-3}$	0 %
b) Insert off	$(4022 \pm 58) \text{ mm}^{-3}$	+1.4 %
c) Digital electronics on (120 W)	$(3918 \pm 47) \text{ mm}^{-3}$	-1.3 %
d) All electronics on (300 W)	$(3859 \pm 59) \text{ mm}^{-3}$	-2.7 %
e) + Data Readout	$(3772 \pm 32) \text{ mm}^{-3}$	-4.9 %

TABLE V
DEVIATION OF THE MEASURED COINCIDENCE RATE FOR DIFFERENT MR SEQUENCES

MR sequence	Coincidence rate deviation
B_0 only	$(0.00 \pm 0.20) \%$
T1-Flash	$(-0.37 \pm 0.20) \%$
T2-TurboRare	$(-0.49 \pm 0.20) \%$
EPI-LR	$(-0.26 \pm 0.20) \%$
EPI-HF	$(-0.13 \pm 0.20) \%$

E. HF Noise

The results obtained with the Bruker QA-SNR sequence are summarized in Table IV. With all electronics powered up, the insert requires about 300-W input power. This resulted in an SNR degradation of 2.7%. During data readout (same power consumption), the degradation increased to 4.9%.

F. Influence of the MRI on PET Coincidence Rate

The measured change of the coincidence rate for different MR sequences is shown in Table V. The change in the coincidence rate is below 0.5% for all tested MR sequences.

G. Images

The first image (Fig. 9) shows a single slice of the hot rod phantom. One can distinguish all rods with 1.7-mm and 2-mm diameter. The 1.5-mm and 1.4-mm rods cannot be separated completely. A profile is shown in Fig. 10.

Fig. 11 shows two slices of an ex vivo rat-brain image taken following an *in vivo* measurement with ^{18}F -labeled tracer (undisclosed). It is an alpha-blended fusion of two stitched

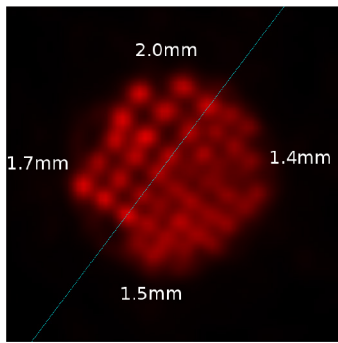


Fig. 9. Hot rod phantom with four different rod-diameters (1.4 mm, 1.5 mm, 1.7 mm, 2.0 mm) and filled with ^{18}F (1.5 MBq/mL). The blue line shows the position of the line profile through the 1.7 mm and 2 mm rods.

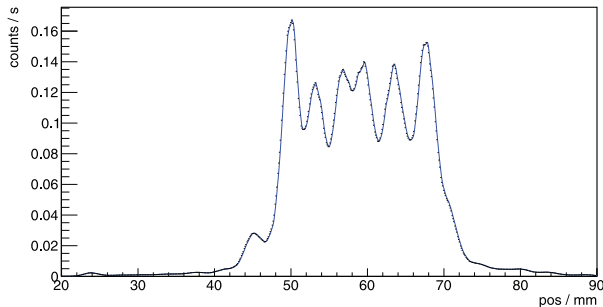


Fig. 10. Line profile through the 1.7 mm and 2 mm rods (see Fig. 9).

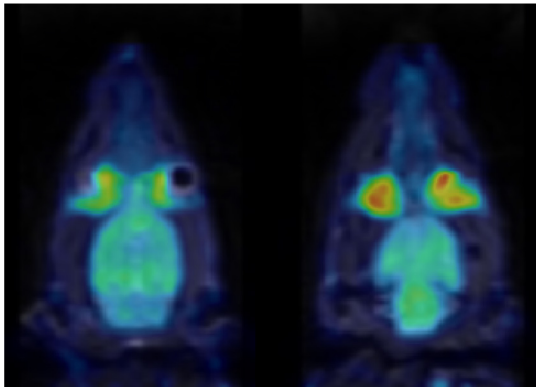


Fig. 11. Two representative slices from a rat brain PET-MR image, 3-D T2 turboRARE (Bruker) MR sequence for anatomical reference, ex vivo PET imaging 1 hr after intravenous ^{18}F brain receptor tracer (undisclosed) injection, image matrix: $36 \times 64 \times 128$; voxel size: $1.0 \text{ mm} \times 0.5625 \text{ mm} \times 0.5 \text{ mm}$, stitch from two PET images (consecutive bed positions). Fusion display of stitched PET (“cold” color table) on MR reference (grayscale).

PET images from consecutive bed positions and one MR image. The first PET image was acquired simultaneously with the MR image and afterward the rat was repositioned for the second PET image. The images match without visible distortion (assessed during image matching in $x/y/z$ planes).

A mouse *in vivo* image with an ^{18}F -labeled tracer (undisclosed) for myocardial perfusion is shown in Fig. 12. A sample slice is shown for an image frame reconstructed with 5-s duration, taken 20 min after injecting 84.9 MBq. One can see clearly the expected shape of the myocardium.

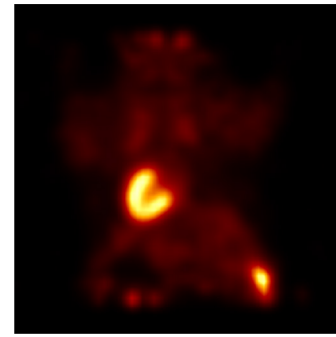


Fig. 12. Mouse *in vivo* PET image, single frame (5 s) at 20 min after intravenous ^{18}F tracer injection, tracer (undisclosed) targets the heart muscle, 84.9 MBq activity, image matrix: $120 \times 120 \times 60$; voxel size: $0.73 \times 0.73 \times 0.73 \text{ mm}$, no concurrent MR image was acquired.

V. DISCUSSION

A. Temperature Measurements

The temperature sensors have an accuracy of 1 K in the range from 0 °C to 85 °C [10]. This matches with the variation of the temperature curves. The spread of the average temperature for different boards was less than ± 1 °C. These observations match with the expectation based on the air-conditioned environment, the constant power consumption of the hardware and constant air flow. The variations in the board temperature are caused by changes of the ambient air temperature origination from the air conditioning system. The measured temperature increase of 5 °C matches with the expected value (5.6 °C) derived from the nominal air flow of the side channel blower (160 m³/h), the heat capacity of air (1.2 kJ/K/m³) and the power dissipation of the electronics [15].

B. PET Results

The photopeak is clearly visible in the coincidence energy spectrum. A limitation for the energy resolution is the number of micro-cells in each SiPM pixel (1580). However, the energy resolution achieved is sufficient for our application. Since the minimum in between the photopeak and the Compton edge is around 390 keV, we selected an energy window from 391 keV to 601 keV for the analysis. To the best of our knowledge, there is no preclinical PET scanner with a better CTR than the reported 194 ps (FWHM) at low activity [16]–[27]. The majority of the 511-keV gamma rays are scattered in the LYSO crystals [28], [29]. Therefore, some of these scattered rays escape the original crystal of interaction and interact again in neighboring crystals. In light-sharing and monolithic detector designs, interactions with intercrystal scatter will create overlapping light patterns. Hence, the detected signal will be a combination of the signals of the individual interactions, if no further filtering is applied. The SAFIR detector system, comprising individually read out crystal elements and a very high data bandwidth, allows to digitize all singles including those of scattered events and to store their data on the DAQ computer. With intercrystal scatter recovery, we observe an increase in the number of detected coincidences by more than 50% compared to the case without intercrystal scatter recovery

and the same energy window. Our algorithm, that identifies the crystal with the highest energy deposit as the crystal of the first interaction, was also successfully applied by other groups [30]–[33].

C. MR Results

The maximum deviation in the B_0 map was 0.7 ppm and inside the shimmed region it was even smaller. This is sufficient for all planned MR-measurements.

We observed a minor degradation of the SNR value during operation of our insert. An increase in the power consumption reduced the SNR by 2.7%. During data readout, the value was decreased in total by 4.9%. Bruker indicates the typical SNR range for this coil/phantom combination to be 2000 mm^{-3} to 2500 mm^{-3} , meaning that even after degradation we are well above the functional SNR.

The coincidence rate does not change significantly during simultaneous PET-MR acquisition (see Table V).

D. Images

In the hot rod phantom, all rods with 2 mm and 1.7 mm can be distinguished clearly. Therefore, one can deduce that similar-sized features in animals can be resolved.

The *ex vivo* rat image consists of two stitched PET images and one MR image. Stitching of the two PET images was straightforward without significant artefacts. The combined PET image matches very well with the MR image.

The *in vivo* mouse image is our first high rate image with an injected activity of 84.9 MBq. This is already two to 20 times the typical activity used in conventional preclinical PET scanners [34], [35]. One can clearly see the expected shape of the myocardium, indicating sufficient image quality for cardiac studies in mice.

VI. CONCLUSION AND OUTLOOK

In this article, we presented the first results obtained with the SAFIR Prototype insert. We achieved an excellent CTR of 194 ps on system level. This exceeds our design goals for the scanner. The same applies to the measured CER of 13.8%. The first PET-MR and high rate images are already of promising quality and indicate that we obtain the spatial resolution required for small animal research applications. We anticipate that applying an improved image reconstruction algorithm will further increase the image quality [36]. The next step is the construction of the full system, with an increased axial field of view (180 mm).

ACKNOWLEDGMENT

The authors thank the “radiopharmaceutical science group at the Institute for Pharmaceutical Sciences of ETH Zurich” for facilitating the *ex vivo* rat study and providing radio tracers.

REFERENCES

- [1] R. Becker *et al.*, “Studies of the high rate coincidence timing response of the STiC and TOFPET ASICs for the SAFIR PET scanner,” *J. Instrum.*, vol. 11, no. 12, 2016, Art. no. 12001.
- [2] R. Becker *et al.*, “The SAFIR experiment: Concept, status and perspectives,” *Nucl. Instrum. Methods Phys. Res. A, Accelerators Spectrometers Detectors Assoc. Equip.*, vol. 845, pp. 648–651, Feb. 2017.
- [3] M. Ahnen *et al.*, “Performance measurements of the SAFIR prototype detector with the STiC ASIC readout,” *IEEE Trans. Radiat. Plasma Med. Sci.*, vol. 2, no. 3, pp. 250–258, May 2018.
- [4] C. Tsoumpas, D. Visvikis, and G. Loudos, “Innovations in small-animal PET/MR imaging instrumentation,” *PET Clin.*, vol. 11, pp. 1051–18, Apr. 2016.
- [5] R. Becker *et al.*, “Monte-Carlo simulation based estimation of NECR, sensitivity, and spatial resolution of a novel preclinical PET insert for MR,” in *Proc. IEEE Nucl. Sci. Symp. Med. Imag. Conf. (NSS/MIC)*, San Diego, CA, USA, Oct. 2015, pp. 1–3.
- [6] X. Zhang *et al.*, “Subsecond total-body imaging using ultrasensitive positron emission tomography,” *Proc. Nat. Acad. Sci.*, vol. 117, no. 5, pp. 2265–2267, 2020.
- [7] R. Dohle *et al.*, “LTCC based highly integrated SiPM module with integrated liquid cooling channels for high resolution molecular imaging,” *J. Microelectron. Electron. Packaging*, vol. 15, no. 2, pp. 86–94, 2018.
- [8] I. Sacco, R. Dohle, P. Fischer, C. Piemonte, and M. Rizet, “A compact, high-density gamma-detection module for time-of-flight measurements in PET applications,” *Nucl. Instrum. Methods Phys. Res. A, Accelerators Spectrometers Detectors Assoc. Equip.*, vol. 824, pp. 233–236, Jul. 2016.
- [9] J. Fischer, “Development of pre-clinical and clinical positron emission tomography detectors,” Ph.D. dissertation, Dept. Phys., Inst. Particle Phys., ETH Zürich, Zürich, Switzerland, 2017.
- [10] *Quad I2C Voltage, Current and Temperature Monitor, Ltc2990*, Analog Devices, Norwood, MA, USA, Nov. 2018.
- [11] C. Ritzer *et al.*, “Compact MR-compatible DC-DC converter module,” *J. Instrum.*, vol. 14, pp. P09016–P09016, Sep. 2019.
- [12] J. Du, J. P. Schmall, M. S. Judenhofer, K. Di, Y. Yong, and S. R. Cherry, “A time-walk correction method for PET detectors based on leading edge discriminators,” *IEEE Trans. Radiat. Plasma Med. Sci.*, vol. 1, no. 5, pp. 385–390, Sep. 2017.
- [13] H. M. Hudson and R. S. Larkin, “Accelerated image reconstruction using ordered subsets of projection data,” *IEEE Trans. Med. Imag.*, vol. 13, no. 4, pp. 601–609, Dec. 1994.
- [14] M. Jacobson *et al.*, “Enhanced 3D PET OSEM reconstruction using inter-update Metz filtering,” *Phys. Med. Biol.*, vol. 45, no. 8, pp. 2417–2439, Jul. 2000.
- [15] E. V. VDI, *VDI-Wärmeatlas*, 11th ed. Heidelberg, Germany: Springer, 2013.
- [16] C. Chang, B. J. Lee, A. M. Grant, A. N. Groll, and C. S. Levin, “Performance study of a radio-frequency field-penetrable PET insert for simultaneous PET/MRI,” *IEEE Trans. Radiat. Plasma Med. Sci.*, vol. 2, no. 5, pp. 422–431, Sep. 2018.
- [17] N. Omidvari *et al.*, “PET performance evaluation of MADPET4: A small animal PET insert for a 7 T MRI scanner,” *Phys. Med. Biol.*, vol. 62, no. 22, pp. 8671–8692, Nov. 2017.
- [18] G. Stortz *et al.*, “Performance of a PET insert for high-resolution small-animal PET/MRI at 7 Tesla,” *J. Nucl. Med.*, vol. 59, no. 3, pp. 536–542, 2018.
- [19] G. B. Ko *et al.*, “Evaluation of a silicon photomultiplier PET insert for simultaneous PET and MR imaging,” *Med. Phys.*, vol. 43, no. 1, pp. 72–83, 2016.
- [20] M. Bergeron *et al.*, “Performance evaluation of the LabPETTM APD-based digital PET scanner,” in *Proc. IEEE Nucl. Sci. Symp. Conf. Rec.*, vol. 6. Honolulu, HI, USA, Oct. 2007, pp. 4185–4191.
- [21] Y. Wang, J. Seidel, B. M. Tsui, J. J. Vaquero, and M. G. Pomper, “Performance evaluation of the GE healthcare eXplore VISTA dual-ring small-animal PET scanner,” *J. Nucl. Med.*, vol. 47, no. 11, pp. 1891–1900, 2006.
- [22] W.-H. Wong *et al.*, “Engineering and performance (NEMA and animal) of a lower-cost higher-resolution animal PET/CT scanner using photomultiplier-quadrant-sharing detectors,” *J. Nucl. Med.*, vol. 53, no. 11, pp. 1786–1793, 2012.
- [23] D. Schug *et al.*, “Initial PET performance evaluation of a preclinical insert for PET/MRI with digital SiPM technology,” *Phys. Med. Biol.*, vol. 61, no. 7, pp. 2851–2878, Apr. 2016.
- [24] J. E. Mackewn *et al.*, “PET performance evaluation of a pre-clinical SiPM-based MR-compatible PET scanner,” *IEEE Trans. Nucl. Sci.*, vol. 62, no. 3, pp. 784–790, Jun. 2015.

- [25] S. España, R. Marcinkowski, V. Keereman, S. Vandenberghe, and R. Van Holen, "DigiPET: Sub-millimeter spatial resolution small-animal PET imaging using thin monolithic scintillators," *Phys. Med. Biol.*, vol. 59, no. 13, pp. 3405–3420, Jun. 2014.
- [26] H. S. Yoon *et al.*, "Initial results of simultaneous PET/MRI experiments with an MRI-compatible silicon photomultiplier PET scanner," *J. Nucl. Med.*, vol. 53, no. 4, pp. 608–614, 2012.
- [27] N. Belcari *et al.*, "Design and detector performance of the PET component of the TRIMAGE PET/MR/EEG scanner," *IEEE Trans. Radiat. Plasma Med. Sci.*, vol. 3, no. 3, pp. 292–301, May 2019.
- [28] C. Ritzer, P. Hallen, D. Schug, and V. Schulz, "Intercrystal scatter rejection for pixelated PET detectors," *IEEE Trans. Radiat. Plasma Med. Sci.*, vol. 1, no. 2, pp. 191–200, Mar. 2017.
- [29] A. Phunpueok, W. Chewpraditkul, V. Thongpool, and D. Aphairaj, "Comparison of photofraction for LuYAP:Ce, LYSO:Ce and BGO crystals in gamma ray detection," in *Proc. 15th Int. Conf. Int. Acad. Phys. Sci.*, Pathumthani, Thailand, Dec. 2012, pp. 1–5.
- [30] Y. Shao, S. R. Cherry, S. Siegel, and R. W. Silverman, "A study of inter-crystal scatter in small scintillator arrays designed for high resolution PET imaging," *IEEE Trans. Nucl. Sci.*, vol. 43, no. 3, pp. 1938–1944, Jun. 1996.
- [31] N. Zeraatkar, M. R. Ay, S. Sarkar, P. Geramifar, and A. Rahmim, "Quantitative investigation of inter-crystal scatter and penetration in the GE discovery RX PET/CT scanner using Monte Carlo simulations," in *Proc. IEEE Nucl. Sci. Symp. Med. Imag. Conf.*, Knoxville, TN, USA, Oct. 2010, pp. 2403–2408.
- [32] J. Clerk-Lamallice, M. Bergeron, C. Thibaudeau, R. Fontaine, and R. Lecomte, "Evaluation of easily implementable inter-crystal scatter recovery schemes in high-resolution PET imaging," in *Proc. IEEE Nucl. Sci. Symp. Med. Imag. Conf. Rec. (NSS/MIC)*, Anaheim, CA, USA, Oct. 2012, pp. 2196–2199.
- [33] M. Rafecas, G. Böning, B. J. Pichler, E. Lorenz, M. Schwaiger, and S. I. Ziegler, "Inter-crystal scatter in a dual layer, high resolution LSO-APD positron emission tomograph," *Phys. Med. Biol.*, vol. 48, no. 7, pp. 821–848, Mar. 2003.
- [34] G. D. Hutchins, M. A. Miller, V. C. Soon, and T. Receveur, "Small animal PET imaging," *ILAR J.*, vol. 49, no. 1, pp. 54–65, Jan. 2008.
- [35] J.-C. Tseng, O. J. Kelada, and J. D. Peterson, *Preclinical In Vivo Imaging PET 101: Best Practices for Preclinical 18 F-FDG PET Imaging*, PerkinElmer, Inc., Hopkinton, MA, USA, 2017.
- [36] P. Khateri, J. Fischer, W. Lustermann, C. Tsoumpas, and G. Dissertori, "Implementation of cylindrical PET scanners with block detector geometry in STIR," *EJNMMI Phys.*, vol. 6, no. 1, p. 15, Jul. 2019.